Confocal light absorption and scattering spectroscopic microscopy

Hui Fang, Le Qiu, Edward Vitkin, Munir M. Zaman, Charlotte Andersson, Saira Salahuddin, Lauren M. Kimerer, Patsy B. Cipolloni, Mark D. Modell, Bradley S. Turner, Sarah E. Keates, Irving Bigio, Irving Itzkan, Steven D. Freedman, Rama Bansil, Eugene B. Hanlon, and Lev T. Perelman

We have developed a novel optical method for observing submicrometer intracellular structures in living cells, which is called confocal light absorption and scattering spectroscopic (CLASS) microscopy. It combines confocal microscopy, a well-established high-resolution microscopic technique, with light-scattering spectroscopy. CLASS microscopy requires no exogenous labels and is capable of imaging and continuously monitoring individual viable cells, enabling the observation of cell and organelle functioning at scales of the order of 100 nm. © 2007 Optical Society of America

OCIS codes: 170.0180, 300.6550.

1. Introduction

In recent decades, we have been witnessing the rapid development of new optical methods both for cell biology, capable of studying living cells and for pathology, capable of *in vivo* tissue diagnosis. The main reason optical techniques have become so popular is because visible and near-infrared light is relatively benign to living cells, thus making it possible to study cells in their natural living conditions. Studying fixed cells with electron microscopy can provide only snapshots of cells at specific time intervals; as a result, very limited information about cell functioning can be extracted from those studies. Being able to study cells in their living conditions and to follow their dynamics is paramount for understanding cell functioning. Techniques that can monitor cells in their natural living conditions will dramatically advance the understanding of diseases and lead to earlier diagnosis.

In studying living cells, confocal fluorescence microscopy is one of the most useful techniques because of its unique optical sectioning properties and also because of the high sensitivity and specificity of fluorescence molecular probes.[1,2] But photobleaching and photodynamic toxicity of exogenous fluorescence probes often make it difficult to monitor cells for long periods of time. Exogenous fluorescence probes may also modify normal cell functioning.[3] To alleviate these problems, significant efforts have recently been made, either to develop new imaging methods, such as two-photon microscopy,[4] that are less prone to the above problems, or to develop new fluorescent protein probes.[5] Optical techniques that rely entirely on intrinsic optical properties of tissue for *in vivo* tissue diagnosis such as confocal reflectance microscopy,[6] optical coherence tomography,[7] light-scattering spectroscopy,[8] and elastic scattering spectroscopy[9] also play a more important role.

Recently an interesting trend has developed. Confocal microscopy has been merging with other optical techniques such as two-photon microscopy,[10] second-harmonic microscopy,[11] or coherent anti-Stokes Raman microscopy.[12] These combined techniques can image tissue deeper than conventional confocal microscopy and at the same time provide enhanced image contrast. Two-photon microscopy can detect autofluorescent molecules such as nicotinamide adenine dinucleotide phosphate (NADH)

H. Fang, L. Qiu, E. Vitkin, M. M. Zaman, C. Andersson, S. Salahuddin, M. D. Modell, B. S. Turner, S. E. Keates, I. Itzkan, S. D. Freedman, and L. T. Perelman (ltperel@bidmc.harvard.edu.) are with the Biomedical Imaging and Spectroscopy Laboratory, Departments of Medicine and ObGyn and Reproductive Biology, Beth Israel Deaconess Medical Center, Harvard Medical School, Boston, Massachusetts 02215. L. M. Kimerer, P. B. Cipolloni, and E. B. Hanlon are with the Department of Veterans Affairs, Medical Research Service and Geriatric Research Education and Clinical Center, Bedford, Massachusetts 01730. I. Bigio and R. Bansil are with the Center for Polymer Studies and the Departments of Physics, Biomedical Engineering and Electrical and Computer Engineering, Boston University, Boston, Massachusetts 02215.

Received 3 July 2006; revised 13 September 2006; accepted 15 September 2006; posted 3 October 2006 (Doc. ID 72575); published 13 March 2007.

0003-6935/07/101760-10$15.00/0

and flavins,[13] second-harmonic microscopy is sensitive to tissue structures with well-defined polarity, such as collagen and microtubules,[14] and coherent anti-Stokes Raman microscopy can detect molecules with specific vibrational modes such as lipids.[15] In addition, several microscopic techniques utilizing backscattering light for tissue diagnosis have been developed recently to image cells on a subcellular level such as optical coherence microscopy[16,17] and elastic scattering spectroscopic microscopy.[18]

Here we report what we believe to be a new type of microscopy called confocal light absorption and scattering spectroscopic (CLASS) microscopy, which combines light-scattering spectroscopy (LSS), recently developed for early cancer detection,[8,19–21] with confocal microscopy. Since CLASS microscopy utilizes backscattered light to detect subcellular structures, it can study living cells without introducing exogenous labels. By combining LSS with confocal microscopy the technique becomes suitable for noninvasive studies of living cells at the subcellular level, whereas previous LSS studies focused primarily on detecting microscopic tissue structures at the cellular level. By using light-scattering spectra of small particles as biomarkers[22,23] CLASS microscopy has the ability to size subcellular organelles on the submicrometer scale beyond the diffraction limit. It appears that LSS spectroscopic signatures of different types of organelle are sufficiently different owing to the characteristic sizes and shapes of organelles.[24,25] Because of that, CLASS microscopy should be capable of differentiating various types of organelle inside the living cell in real time, which is still a challenge for multicolor fluorescence imaging.[26]

Section 2 outlines the principles of CLASS microscopy and provides the method to calculate the CLASS spectra and the method of extracting the size information of organelles from the spectra. Section 3 details the experimental apparatus. Section 4 provides the details of the performed experiments and results. Section 5 provides the discussion and conclusion.

2. Theory

A. Principles of CLASS Microscopy

Recently it was demonstrated[24] that by illuminating an aqueous solution of subcellular organelles with visible and near-infrared light and detecting the light scattering spectra reflected from the solution we can extract information about the size of the organelles with sizing accuracy beyond the diffraction limit. Here we combine LSS with confocal microscopy to create a technique capable of detecting and characterizing individual organelles in a living cell. Since light scattered by structures outside the confocal volume is mostly blocked by the confocal pinhole, confocality makes it possible to study light scattering from a single organelle inside a tiny, femtoliter volume. In this arrangement the entire cell can then be imaged by point-by-point scanning.

However, the geometries of light scattering in the CLASS microscope and in the LSS system are somewhat different. The CLASS microscope collects light scattered at a large range of angles with the maximum angle bounded by the NA of the objective, whereas the LSS system usually collects only light backscattered near a 180° angle. Therefore the CLASS microscope deals with light scattering with significant angular averaging, and its spectra might be quite different from the LSS spectra. To compare the LSS and CLASS spectra we developed an analytical model capable of modeling the CLASS spectra for a wide range of parameters (see Subsection 2.B). From Fig. 1 it is clear that the deviation of the CLASS spectra from the LSS spectrum increases with the increase in NA of the objective. Higher NA means higher spatial resolution, while the decrease in the amplitude of the oscillations means a decrease of the spectroscopic contrast for the sizing accuracy. Therefore there is clearly a trade-off between the spatial resolution and the sizing accuracy determined by the NA of the objective and choosing an objective with an intermediate NA such as 0.5 presented in this paper is a compromise that can balance the spatial resolution for locating the organelles and sizing accuracy for differentiating organelles. Also, as can be seen from Fig. 1, when the size of the scatterers decreases and becomes smaller than 50 nm the Rayleigh scattering regime is reached, and the curves for the different NA converge to the standard λ^{-4} law, where λ is the wavelength.

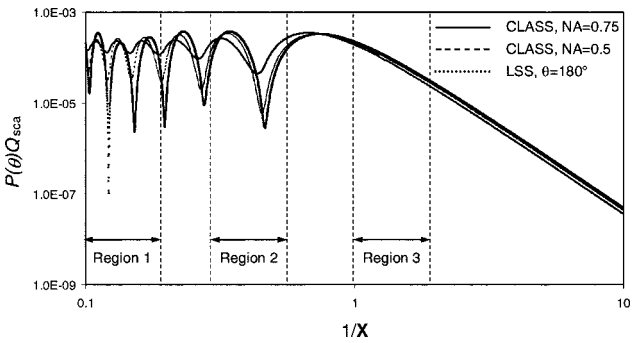

Fig. 1. Comparison of a standard LSS spectrum with two CLASS spectra calculated using Eq. (6). The spectra are presented on a composite graph of the differential scattering coefficients for spherical particles in range of diameters from 20 to 900 nm and wavelength range from 400 to 800 nm versus inverse size parameter $1/x = \lambda/(2\pi a)$. Region 1 shows the spectra over the wavelength range from 400 to 800 nm for 900 nm particles. Regions 2 and 3 show the spectra over the same wavelength range for 300 nm particles and for 100 nm particles, respectively. All the spectra are calculated for the case of a spherical particle with a relative refractive index of $n = 1.06$ surrounded by the medium with a refractive index equal to 1.36. The dotted curve is a LSS spectrum with a scattering angle of 180°, the dashed curve is a CLASS spectrum with a NA of 0.5, and the solid curve is a CLASS spectrum with a NA of 0.75. On the right side of the graph all three curves converge to a $1/\lambda^4$ Rayleigh scattering behavior.

B. Calculation of CLASS Spectra

Since the experimentally measured CLASS spectrum of a cell is a linear combination of the CLASS spectra of various subcellular organelles with different sizes

and refractive indices within the cell, to extract these parameters, we can express the experimental spectrum as a sum over the organelles' diameters and refractive indices:

$$S(\lambda,\ \mathrm{NA}) = \int_0^\infty I\left(\frac{\lambda}{\delta},\ n,\ \mathrm{NA}\right)N(\delta)\mathrm{d}\delta + \varepsilon(\lambda), \quad (1)$$

where $S(\lambda, \mathrm{NA})$ is the experimental spectrum collected with an objective having a NA, $N(\delta)$ is the organelles' size distribution, $I(\delta/\lambda, n, \mathrm{NA})$ is the CLASS spectrum of a single scatterer with diameter δ and relative refractive index n, and $\varepsilon(\lambda)$ is the experimental noise. In realistic situations the lower and upper limits of integral (1) should be modified. For scatterers smaller than some critical value δ_R, integral (1) exhibits Rayleigh behavior and can be approximated with a term proportional to $1/\lambda^4$. In addition, for scatterers larger than the size of the biggest organelle $\delta_{\max}$, there is no contribution to integral (1). Then integral (1) can be written as a discrete sum over the organelles' diameters:

$$\hat{S}(\lambda,\ \mathrm{NA}) = \frac{C_R}{\lambda^4}N_R + \sum_{\delta_R}^{\delta_{\max}}\hat{I}\left(\frac{\lambda}{\delta},\ n,\ \mathrm{NA}\right)\hat{N}(\delta) + \hat{E}(\lambda), \quad (2)$$

where $\hat{N}(\delta) = N(\delta)\mathrm{d}\delta$ is a discrete size distribution, $\hat{S}$ is the experimental spectrum measured at discrete wavelength points, $\hat{I}$ is the CLASS spectrum of a single scatterer, and $\hat{E}$ is the experimental noise. The first term here represents the contribution of Rayleigh scatterers. To extract this size distribution, it is convenient to write this in matrix form:

$$\hat{S} = \hat{I}\cdot\hat{N} + \hat{E}. \quad (3)$$

We use the scalar wave model similar to one developed by Weise *et al.*[27] and Aguilar *et al.*[28] to calculate the CLASS spectrum of a single scatterer $\hat{I}$. In this model the incident and scattering waves are expanded into a set of plane waves with directions limited by the NA of the objective. The amplitude of the signal from a single scatterer is

$$A(\mathbf{R}) = \int_\Omega\int_\Omega P(-\hat{\mathbf{k}})P(\hat{\mathbf{k}}')\exp\left(i\,\frac{2\pi}{\lambda}\,\mathbf{R}(\hat{\mathbf{k}}' - \hat{\mathbf{k}})\right) \times f\left(\frac{\delta}{\lambda},\ n,\ \hat{\mathbf{k}},\ \hat{\mathbf{k}}'\right)\mathrm{d}\hat{\mathbf{k}}\mathrm{d}\hat{\mathbf{k}}', \quad (4)$$

where $\mathbf{R}$ is a position vector of the scatterer relative to the focus, λ is the wavelength of both the incident and the scattered light (since only elastic scattering is considered), $\hat{\mathbf{k}}$ is a unit vector in the direction of propagation of the incident light, $\hat{\mathbf{k}}'$ is a unit vector in the direction of propagation of the scattered light, $P(\hat{\mathbf{k}})$ is the objective pupil function (the same pupil function is used twice to describe light delivery and collection), and $f(\delta/\lambda, n, \hat{\mathbf{k}}, \hat{\mathbf{k}}')$ is the far-field scattering amplitude of the wave scattered in direction $\hat{\mathbf{k}}$ created by the incident wave coming from direction $\hat{\mathbf{k}}'$, and Ω is the solid angle subtended by the objective and is related to its NA. We use Mie theory to calculate the amplitude $f(\delta/\lambda, n, \hat{\mathbf{k}}, \hat{\mathbf{k}}')$.

The calculations can be simplified by considering a particle at the center of the focus, i.e., when $\mathbf{R} = 0$. Then the phase term in Eq. (4) is unity and we get

$$A(0) = \int_\Omega\int_\Omega P(-\hat{\mathbf{k}})P(\hat{\mathbf{k}}')f\left(\frac{\delta}{\lambda},\ n,\ \hat{\mathbf{k}},\ \hat{\mathbf{k}}'\right)\mathrm{d}\hat{\mathbf{k}}\mathrm{d}\hat{\mathbf{k}}'. \quad (5)$$

To compare with the measured CLASS spectrum of a single scatterer, we calculate the scattering intensity, which is the square of the amplitude, and relate it to the intensity of the incident light at each wavelength. This gives the following spectral dependence of the CLASS signal:

$$I\left(\frac{\delta}{\lambda},\ n,\ \mathrm{NA}\right) = \frac{|A(0)|^2}{I_0} = \frac{\left|\int_\Omega\int_\Omega P(-\hat{\mathbf{k}})P(\hat{\mathbf{k}}')f\left(\frac{\delta}{\lambda},\ n,\ \hat{\mathbf{k}},\ \hat{\mathbf{k}}'\right)\mathrm{d}\hat{\mathbf{k}}\mathrm{d}\hat{\mathbf{k}}'\right|^2}{\left|\int_\Omega\int_\Omega P(-\hat{\mathbf{k}})P(\hat{\mathbf{k}}')\mathrm{d}\hat{\mathbf{k}}\mathrm{d}\hat{\mathbf{k}}'\right|^2}. \quad (6)$$

To check this expression we can consider the case of isotropic scattering. In this case f is a constant and $I = f^2$ as it is supposed to be. Another limiting case is when NA is close to 0 and we get $I = |f(\hat{\mathbf{k}}, \hat{\mathbf{k}})|^2$ as it should be for the backscattering coefficient in the exact backward direction.

Figure 1 provides a comparison of a standard LSS spectrum with two CLASS spectra calculated by using Eq. (6). All spectra are calculated for the case of a spherical particle with relative refractive index $n = 1.06$ surrounded by a medium with refractive index equal to 1.36. Those parameters are close to the parameters of an organelle surrounded by cytoplasm. The two CLASS spectra are calculated for the objectives with a NA of 0.5 and NA of 0.75.

Even though at a NA of 0.75 the CLASS spectra still have sufficient structure and contrast to differentiate the sizes of the scatterer, to optimize the spatial resolution to locate the organelles and sizing accuracy to differentiate organelles in the prototype CLASS microscope we chose the objective with a NA of 0.5.

C. Extraction of Particle Sizes

For given relative refractive index n $I(\delta/\lambda, n, \mathrm{NA})$ is a function of a single variable δ/λ. After calculating it

for the particular optical arrangement of the CLASS microscope we formed a matrix $\hat{I}$ with λ varying along columns and δ along rows. For the biologically reasonable range of sizes and refractive indices, the matrix $\hat{I}$ was calculated and stored for future use. We chose a lower limit of $\delta_R = 100$ nm and an upper limit of $\delta_{max} = 7$ μm. The lower limit is at the transition to Rayleigh behavior since scatterers smaller than δ_R exhibit behavior proportional to $1/\lambda^4$, and contributions from those scatterers are described as a separate term. The origin of the Rayleigh term could come from very small particles present in a cell and also from large protein macromolecules.

Since the CLASS spectrum $\hat{I}$ is a highly singular matrix and a certain amount of noise is present in the experimental spectrum $\hat{S}$, it is not feasible to calculate size distribution $\hat{N}$ by directly inverting matrix $\hat{I}$. Instead we can multiply both sides of the equation $\hat{S} = \hat{I} \cdot \hat{N} + \hat{E}$ by the transpose matrix $\hat{I}^T$ and introduce the matrix $\hat{C} = \hat{I}^T \cdot \hat{I}$. We can now compute the eigenvalues $\alpha_1, \alpha_2, \ldots$ of matrix C and sequence them from large to small. This can be done because $\hat{C}$ is a square symmetric matrix. Then we will use the linear least squares with the nonnegativity constraints algorithm[29] to solve

$$\hat{I}^T\hat{S} - (\hat{C} + \alpha_k\hat{H})\hat{N} \rightarrow \min, \quad \hat{N} \geq 0, \tag{7}$$

where $\alpha_k\hat{H}\hat{N}$ is the regularization term, and matrix $\hat{H}$ represents the second derivative of the size distribution. The use of the nonnegativity constraint and the regularization procedure is critical to finding the correct distribution $\hat{N}$.

To solve the system of expressions (7) we developed a Fortran code that uses the LCLSQ routine for linear least-square problems with linear constraints from the International Mathematical and Statistical Library (MSL).[30,31] By using this algorithm we accurately reconstruct the size distributions of the scattering particles (microspheres and organelles) present in the focal volume of the CLASS instrument.

3. Experimental Setup

A schematic of the prototype CLASS microscope is shown in Fig. 2(a). In this system, light from a broadband source is delivered through an optical fiber (200 μm diameter, NA of 0.22) to a 30 μm pinhole. The delivery optical fiber is terminated in a fiber chuck and mounted in a fiber positioner that allows a precise alignment of the fiber relative to the pinhole by using an alignment laser. An iris diaphragm positioned behind the pinhole is needed to limit the beam divergence and to prevent any stray light reflected toward the detector. The size and position of the iris diaphragm are chosen so that the diameter of the divergent beam (~20 mrad) matches the objective pupil of the fixed tube length reflective objective. The light beam from the delivery pinhole is transmitted through the beam splitter (Newport) and the achromatic reflective objective (NA of 0.5, 36× magnification, Ealing 25-0522). Since CLASS is a multiwavelength spectroscopic technique, an achromatic reflective objective and a broadband beam splitter are used.

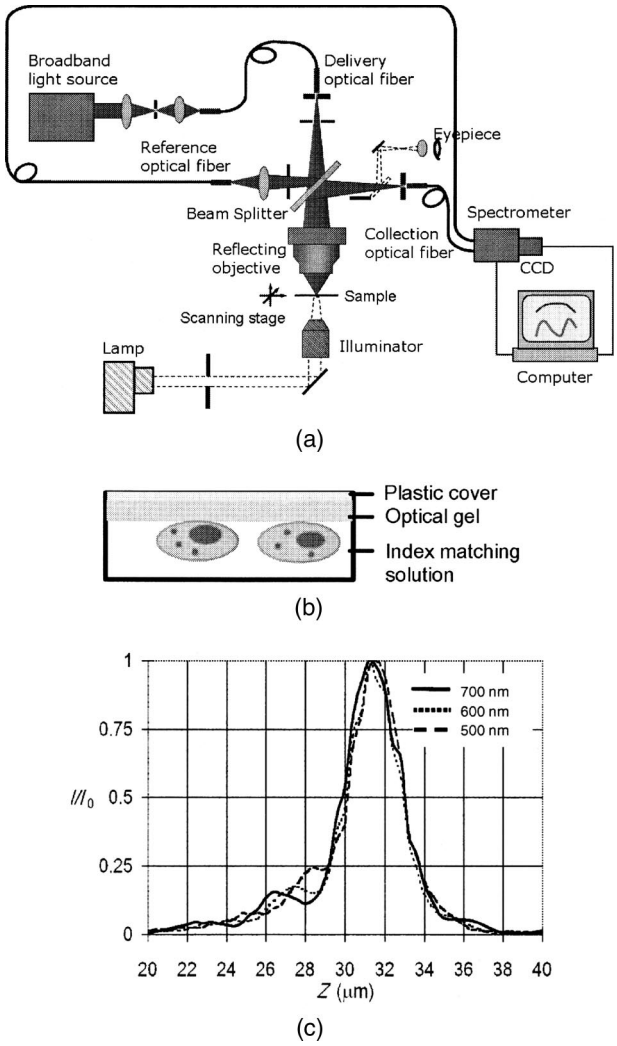

Fig. 2. (a) Schematic of the prototype CLASS microscope, (b) cell imaging chamber, (c) depth sectioning at three wavelengths.

The sample is placed in an imaging chamber as shown in Fig. 2(b). The chamber was assembled from elements of two standard imaging chambers (Grace Bio-Lab, Bend, Oregon, PCI-A-0.5). The chambers have a 20 mm internal diameter, a 0.5 mm depth, and a plastic cover with a thickness of 0.1 mm. We placed optical gel (Fiber Optic Center, LS-3238) on the inside surface of the cover of one of the imaging chambers. After curing, the optical gel forms a layer of approximately 0.2 mm thickness that matches the refractive index of the solution in the chamber. The chamber is mounted on the *XYZ* motorized translation stage (Thorlabs MT-Z6), and the sample is imaged by point-by-point scanning. The stage is equipped with dc servo actuators and optical encoders and has a 40 nm resolution in each direction.

Light backscattered from the sample is collected by the same objective and is reflected by the beam splitter toward the 30 μm collection pinhole. Between the beam splitter and the pinhole there is a mirror that can flip into the light path to redirect light from the sample to an eyepiece. This arrangement adds an extra ocular function to the CLASS system and allows us to observe a visual image of the target using transmission from a cw Xe arc lamp (100 W cw, Oriel Instrument) in an arrangement similar to a conventional transmitting microscope [Fig. 2(a)]. The collection pinhole limits the light coming from regions above and below the focal plane, allowing only the light scattered from a small focal volume to pass. The light passing through the pinhole is directed to the spectrometer optical fiber (100 μm diameter, NA of 0.11) coupled to the SpectraPro-150 imaging spectrometer (Acton Research, Acton, Massachusetts) and TE-cooled detector (DU-434-FI Andor Technology, South Windsor, Connecticut). The spectrometer has a 480–960 nm spectral bandwidth and a 4 nm spectral resolution. The data from the detector are transferred to the computer, which also controls the three-axis motorized translation stage. A separate reference fiber [see Fig. 2(a)] samples source light from the beam splitter and delivers this light to the imaging spectrometer. This light is imaged onto a separate track of the CCD and is used to correct for intensity and spectral variations of the light source during image acquisition time.

The light source for the CLASS microscope is critical since (1) its spectral range determines the limits of extraction accuracy for subcellular organelle features using the LSS spectra and (2) its brightness limits the system signal-to-noise ratio (SNR), thus the speed of data acquisition for a given accuracy of extraction. The system design has two options for broadband illumination: either a Xe arc lamp used for measurements performed on extracted organelles in suspension or a supercontinuum laser source used for measurements performed on organelles in living cells. The lamp source provides stable, cw operation over a very wide spectral range while the supercontinuum source provides very high brightness enabling near-real-time acquisition of images.

We developed a real-time LabVIEW code with a graphic user interface in the environment of LabVIEW 7.1 (National Instruments, Austin, Texas) to control the entire system. The code initializes and controls the temperature of the CCD, sets up the CCD capturing regime, and tracks positions for the signal and reference fibers in the multitrack regime. During the multispectral image acquisition the code simultaneously controls and synchronizes the raster scan of the target performed with the motorized translation stage and the data collection with the CCD detector.

In our early experiments with the CLASS instrument we established its depth sectioning characteristics by scanning a mirror along the objective optical axis at three different wavelengths [Fig. 2(c)]. The half-width of the detected signal is approximately 2 μm, which is close to the theoretical value for a 30 μm pinhole and a 36× objective.[32] In addition, the shapes of all three spectra (500, 600, and 700 nm) are similar, which demonstrates the good chromatic characteristics of the instrument.

4. Results

We performed three sets of experiments with the prototype CLASS microscope. In the first set we measured polystyrene beads in suspensions to calibrate the microscope and to test the size extraction algorithm. In the second set we measured distributions of organelle sizes in aqueous solutions and compared these distributions to distributions measured using electron microscopy. The purpose of these experiments was to check the ability of CLASS microscopy to uniquely identify various types of organelle by their light-scattering spectra. The third set of experiments involved the imaging of individual living cells and time sequencing experiments with those cells. Specifically, we studied apoptotic changes in human bronchial epithelium cells and also imaged mucin granules in an AGS gastric epithelial cell.

A. Experiments with Suspensions of Polystyrene Beads

To calibrate the system we performed experiments with polystyrene bead suspensions. We created samples by mixing beads of two different sizes in water and in glycerol. We used two sizes of beads to establish that the technique can separate particles of multiple sizes, and we used glycerol in addition to water because the relative refractive index of the polystyrene beads in water (n_r = 1.194 at 600 nm) is substantially higher than that of subcellular organelles in cytoplasm, which is in the range of n_r = 1.03–1.1 at visible wavelengths. By suspending the beads in the glycerol we can decrease their relative refractive index to 1.07–1.1 in the visible range, a closer approximation to the biological ratio. (The refractive index of polystyrene can be accurately described by the expression $n = 1.5607 + 10{,}002/\lambda^2$ where λ is in nanometers.[33])

We mixed the beads with a mean size of δ_1 = 175 nm and a standard deviation of 10 nm with the beads with a mean size of δ_2 = 356 nm and a standard deviation of 14 nm. In the water suspension the number density of 175 nm beads was $0.5/\mu m^3$, and the number density of 356 nm beads was $0.0625/\mu m^3$. In the glycerol suspension the number density of 175 nm beads was $1/\mu m^3$, and the number density of 356 nm beads was $0.125/\mu m^3$.

Figure 3(a) shows the CLASS spectra of polystyrene bead mixtures in water and glycerol and a comparison with the theoretical fits. In these experiments Brownian motion moved the beads in and out of the microscope focus. Therefore the data were taken by averaging over a large number of beads. This was necessary to improve the statistics of the measurements. The difference between the experiments and the theory is less than 1% for both cases.

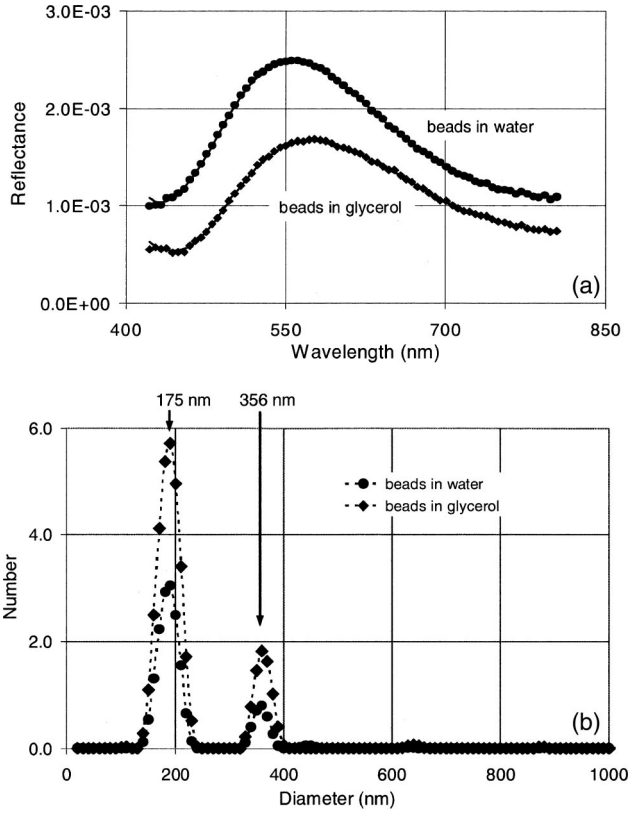

Fig. 3. (a) CLASS spectra and (b) extracted size distributions for polystyrene beads in water and glycerol. Dots, experimental data; solid curves, spectra reconstructed from the theoretical model; points, calculated values; dotted curves, a guide for the eye.

Figure 3(b) shows the extracted size distributions. The parameters of the extracted size distributions are close to the parameters provided by the manufacturer (see Table 1). For example, the extracted mean sizes of the 175 nm beads are within 15 nm of the manufacturer's sizes, and the mean sizes of the 356 nm beads are even better, within 4 nm of the manufacturer's sizes.

We also scanned twelve individual submicrometer polystyrene beads, four 535 nm beads, four 771 nm beads, and four 1053 nm beads whose sizes were given by the manufacturer. In these experiments the bead was in contact with the plastic cover of the imaging chamber and scanned point by point. The image

Table 1. Size Distribution Parameters for Polystyrene Beads

	Size 1		Size 2	
	Mean Size (nm)	Standard Deviation (nm)	Mean Size (nm)	Standard Deviation (nm)
Manufacturer's data	175	10	356	14
CLASS Microscopy in water	185	40	360	30
CLASS Microscopy in glycerol	190	40	360	30

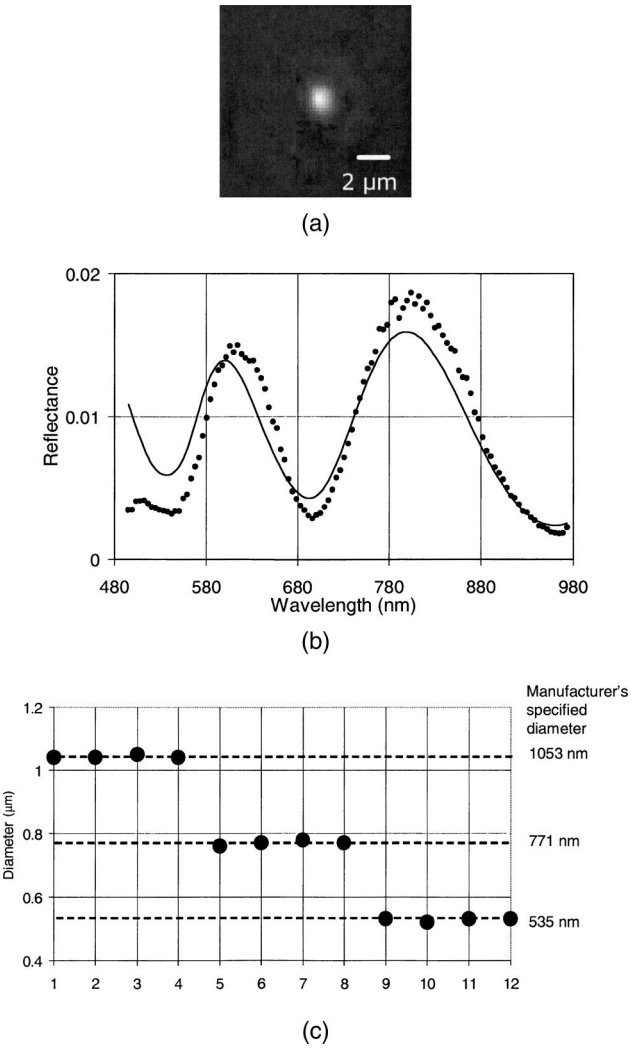

Fig. 4. (a) Image of a 771 nm diameter polystyrene bead at a wavelength of 600 nm, (b) comparison of the CLASS spectrum collected at the center of the bead (dotted curve) with calculated spectrum (solid curve), (c) reconstructed sizes of 12 individual beads. The CLASS measurements are all within 10 nm of the manufacturer's specified sizes.

of the 771 nm bead at the wavelength of 600 nm is shown in Fig. 4(a). The spectrum of the same bead at its center is shown in Fig. 4(b) as dots, and the model fit is shown as a solid curve. For all 12 beads the reconstructed sizes are presented in Fig. 4(c), and the CLASS measurements are all within 10 nm of the manufacturer's specified sizes.

B. Experiments with Organelle Suspensions

We performed measurements on suspensions of rat liver cell organelles. Rat liver cells were subfractionated using stepped differential and density gradient centrifugation following the protocol described in Ref. 34. Briefly, adult rats were sacrificed by asphyxiation, under an institutionally approved protocol. The liver was minced with scissors, suspended in 0.25 M phosphate-buffered saline (PBS) and homogenized in a Dounce homogenizer on ice. The homogenate then

underwent stepped differential and density gradient centrifugation procedures to obtain purified fractions enriched in mitochondria, peroxisomes, and microsomes and a light mitochondrial fraction composed of both mitochondria, peroxisomes, and some lysosomes. Each fraction of viable organelles thus obtained was separated into two specimens, one for CLASS measurements and one for electron microscopy (EM). The CLASS specimens were used without further preparation as a suspension in the aqueous glucose solution of the final isolation step. The EM specimens were fixed in 2.5% glutaraldehyde in phosphate buffer, postfixed in cold 1% osmium tetroxide, poststained with alcoholic uranyl acetate, and embedded in fresh Epon Araldite. The orientation chosen for sectioning the cell fractions was normal to the gradient that resulted from centrifuging. Thin sections of approximately 60 to 80 nm were prepared and photographed with a Phillips 200 electron microscope at both low and high magnification. In cases where there were particles of varying sizes present, all were photographed.

The suspended organelles were placed in a glass tube. The density of the suspension was approximately 1 per 1 cubic μm. In a separate light-scattering experiment with the fiber optic setup described in Ref. 24, the scattering coefficient of the suspension was determined to be 4 mm^{-1}. The CLASS measurements were performed with the beam focused approximately 25 μm below the glass–PBS interface to minimize interference from the tube wall. To measure statistically reliable distributions of the organelle sizes we made the exposure time long enough to allow the organelles to move in and out of the confocal volume because of the Brownian motion. For the 100 W Xe arc lamp source the exposure time of the typical measurements took approximately 100 s with the distributions averaged over several hundreds of organelles.

The results for a typical experiment are presented in Fig. 5. In this experiment the mixture of two types of organelle, microscomes and peroxisomes, was measured with CLASS microscopy and EM. The electron micrograph of the mixture [Fig. 5(a)] taken at 63,492 magnification clearly shows the presence of larger peroxisomes and smaller microscomes in the field of view. The EM morphological measurements were performed by overlaying the electron micrograph image with a 100 nm step grid and counting particles of various sizes. We estimate the accuracy of the counting to be approximately 20 nm. For nonspherical particles we used a mean diameter as the diameter presented in Fig. 5(b). It should be pointed out that electron micrographs provided thin section results since the thickness of the electron microscope sample (60 to 80 nm) is smaller than the size of the particles being measured. To compare EM results with CLASS results, we took into account the frequency of appearance of particles of different sizes in the thin sections and remapped the 3D CLASS size distribution to a 2D EM distribution.

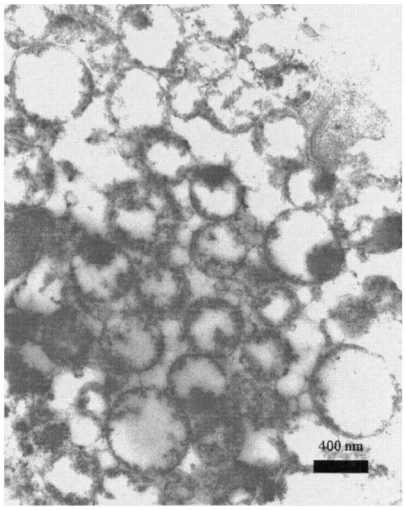

(a)

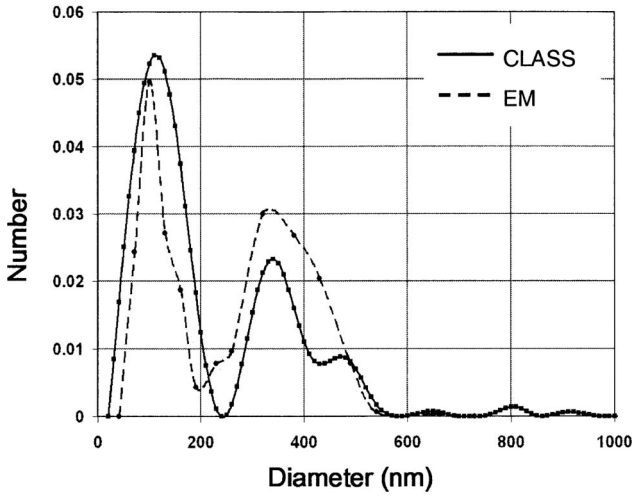

(b)

Fig. 5. Mixture of two types of organelle, microsomes and peroxisomes. (a) Electron micrograph of the mixture taken at 63,492 magnification and (b) comparison of the distribution reconstructed with CLASS microscopy and with EM morphometry performed on the same fraction. Both distributions clearly show two groups of organelle, microsomes and peroxisomes.

We compared the CLASS results with the EM morphometry performed on the same fraction. The corresponding size distributions are presented in Fig. 5(b). The CLASS size distribution clearly shows two groups of organelles, one with sizes ranging from 200 to 500 nm, which appears to be in good agreement with size distribution of peroxisomes obtained with EM, and the other one with sizes below 200 nm, which can be identified as microsomes from EM measurements. The position of the peaks of the mixture measured with CLASS microscopy agrees with the position of the peaks measured with EM to within 10%.

C. CLASS Imaging of Living Cells

To demonstrate the ability of the CLASS microscope to monitor unstained living cells on a submicrometer

scale we studied two types of cell: human bronchial epithelial cells undergoing apoptosis and mucous AGS cells. Live 16HBE14o- human bronchial epithelial cells were cultured in minimal essential medium (Gibco, Grand Island, New York) with 10% fetal bovine serum, penicillin 100 unit/ml and streptomycin 100 μg/ml. Cells (50% confluent) were incubated with 100 μM docosahexaenoic acid (DHA) for 24 h to induce apoptosis. Then the cells were detached with trypsin/EDTA, washed in Dulbecco's modified eagle medium (DMEM) solution without phenol red and resuspended in the DMEM/OptiPrep solution. The cells suspended in the 1:1 solution prepared by mixing OptiPrep (Axis-Shield) with DMEM are placed in the imaging chamber described in Section 3. Since optical gel has a refractive index of 1.384 at 589 nm wavelength, and the solution of the OptiPrep and DMEM has a refractive index of 1.382, the reflections from the gel–liquid interface are minimal.

Figure 6 presents CLASS images of two 16HBE14o- cells. The images on the left are of a normal untreated cell, and images on the right are of a cell treated for 24 h with DHA, an agent for inducing apoptosis. Figure 6(a) presents unprocessed cross-sectional images of the cells collected with the CLASS microscope at 640 nm wavelength. The images of the same cells reconstructed from the CLASS microscope spectra are presented in Fig. 6(b). The diameters of the spheres in the image represent the reconstructed sizes of the individual organelles as determined from their spectra, the gray scale represents their refractive indices, and the positions are identified from the maxima of the CLASS signals. Individual organelles can easily be identified inside the cell. In the cells on the right, undergoing apoptosis, the organelles form shell-like structures with an empty space in the middle, the classic shape for apoptotic cells. The treated and untreated cells show clear differences in organelle spatial distribution.

Information about each location inside the cell is reconstructed from the typical spectra presented in Fig. 6(c). Here dotted curves represent experimental results, and solid and dashed curves represent theoretical fits. The spectra show oscillations with periodicity related to the sizes of the organelles in the confocal volume. For example, the spectrum represented by the dashed curve shows higher frequency oscillations that correspond to mitochondria, a larger organelle with a size in the 700–1100 nm range. The spectrum represented by the solid curve shows lower frequency oscillations that correspond to a peroxisome, a smaller organelle whose size and shape were reconstructed as a sphere with approximately a 400 nm diameter.

In the second set of experiments AGS gastric epithelial cells (American Type Culture Collection, Rockville, Maryland) were grown in F-12 Ham's medium (pH 7.4: Sigma-Aldrich) supplemented with 10% fetal bovine serum, 100 units/ml penicillin G sodium, and 100 μg/ml streptomycin sulfate. All cultures were maintained at 37 °C in a humidified atmosphere of 95% air and 5% CO_2. Then the cells were

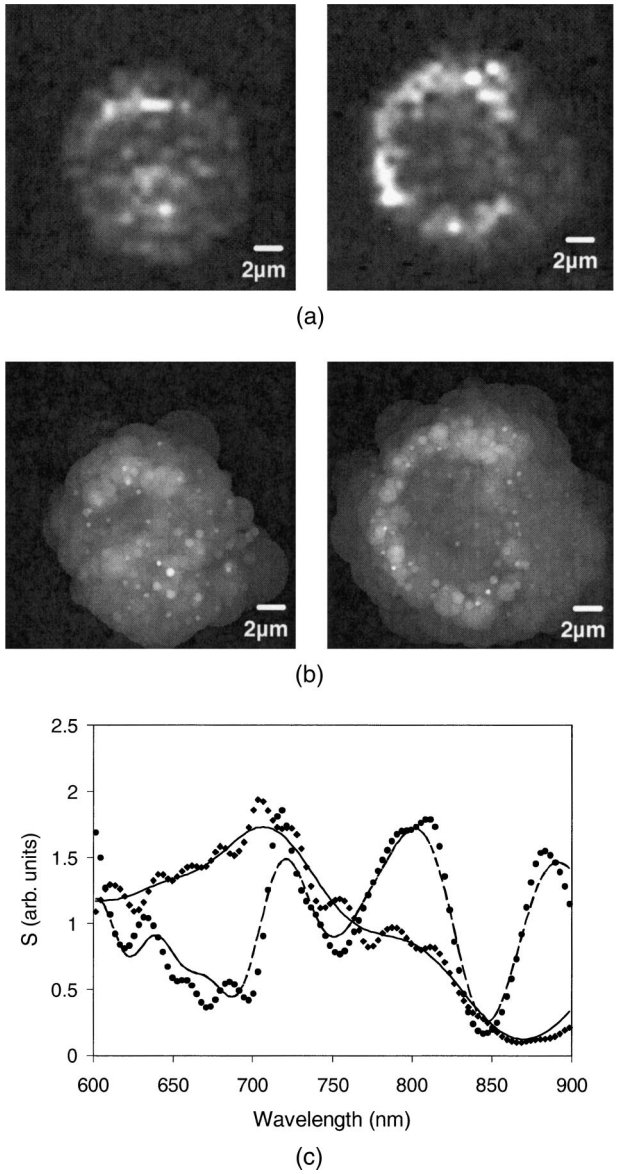

Fig. 6. (a) Unprocessed cross-sectional images of two 16HBE14o- human bronchial epithelial cells collected with the CLASS microscope at 640 nm wavelength. The left cell is a normal untreated cell and the right cell was treated with DHA for 24 h and is undergoing apoptosis. (b) Images of the same cells reconstructed from the CLASS microscope spectra. The diameters of the spheres in the image represent the reconstructed sizes of the individual organelles, and the gray scale represents their refractive indices. (c) CLASS spectra taken from two different locations in a cell: dotted curves, experimental results; solid and dashed curves, theoretical fits. The spectra show oscillations with periodicity related to the size of the organelle in the confocal volume.

detached with trypsin/ethylenediaminetetraacetate (EDTA), washed in DMEM without phenol red and resuspended in the gradient solution with 1:1 DMEM and OptiPrep.

In addition to the organelles, mucous cells have mucin granules that have a rounded shape and size in the range of 0.5–2 μm. These granules can be detected inside the mucous cell when labeled with a molecular marker, for example, FITC-labeled antibody[35] and

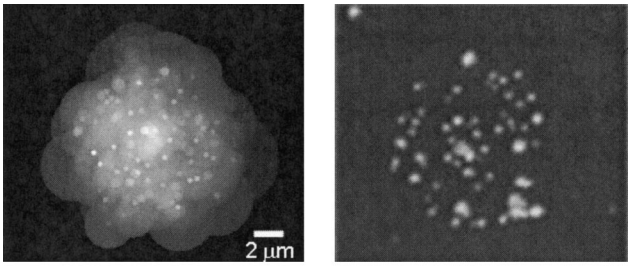

Fig. 7. (a) Cross-sectional image of an AGS gastric epithelial cell reconstructed from the CLASS microscope spectra. Mucin granules are clearly seen. (b) Fluorescence-based image of the same type of cell from Ref. 35 with mucin granules labeled by a FITC antibody.

imaged with fluorescence microscopy. We performed CLASS microscopy measurements on a mucous cell and created the reconstructed image presented in Fig. 7(a). The fluorescence-based image of the same type of cell from paper[35] with mucin granules labeled by fluorescein isothiocyanate (FITC) antibody is presented in Fig. 7(b). Both images show a tightly packed mass of particles of similar size which represent mucin granules.

5. Discussion and Conclusion

We have presented the results of studies that show that CLASS microscopy is capable of reconstructing images of living cells with submicrometer resolution without the use of exogenous markers. Fluorescence microscopy of living cells requires the application of molecular markers that can affect normal cell functioning. In some situations, such as studying embryo development, the phototoxication caused by fluorescent tagged molecular markers is not only undesirable but unacceptable. Another potential problem with fluorescence labeling is that multiple fluorescent labels may have overlapping line shapes, and this limits the number of species that can be imaged simultaneously in a single cell. CLASS microscopy is not affected by those problems. It requires no exogenous labels and is capable of imaging and continuously monitoring individual viable cells, enabling the observation of cell and organelle functioning at scales of the order of 100 nm. CLASS microscopy can provide not only size information but also information about the biochemical and physical properties of the cell since light-scattering spectra are sensitive to absorption coefficients and the refractive indices, which in turn are directly related to the organelle's biochemical and physical composition (such as the chromatin concentration in nuclei or the hemoglobin concentration and oxygen saturation in red blood cells).

We used a scalar wave model to take into account the confocal properties of the CLASS microscope and Mie theory to calculate the scattering amplitude. More rigorous models[36] that take into account the deviation from the spherical shapes of some of the organelles and the vector nature of the electric field can improve CLASS reconstruction abilities. In addition, for densely packed scattering particles there is the possibility of observing interference effects in the light scattered from adjacent particles. This must be taken into account in reconstructing scattering particle properties from CLASS spectra in dense systems. However, this cross term has not been significant for the organelle and microsphere densities in the experiments reported here. We are currently working on incorporating the discrete dipole approximation and the Rayleigh–Gans approximation in our models. However, our present studies with organelle suspensions clearly indicate that the approximations we are using can provide accurate and useful results.

In conclusion, we have described a novel technique, called confocal light absorption and scattering spectroscopic microscopy, for use in the noninvasive dynamic monitoring of subcellular structures. Potential applications include multiple areas of biomedical research. The CLASS microscope scans biological cells with a focused broadband beam and collects elastically scattered light using a confocal arrangement. Collected light, elastically scattered by various subcellular organelles and structures, provides real-time information about morphological, biochemical, and physical properties of various regions of the living cell and their functions. To extract this information we developed an algorithm similar to the one used by LSS but which also takes into account the confocal geometry of the incoming and scattered light. Light-scattering spectroscopy and elastic scattering spectroscopy have recently been applied to biological problems and primarily to cancer detection.[8,9,18–25] However, the ability to probe living cells noninvasively and to continuously monitor the subcellular structures inside a cell on a subwavelength scale has not to our knowledge been demonstrated previously.

This work was supported by NIH grant RR017361, NSF grant BES-0116833, and the Department of Veterans Affairs, Office of Research and Development.

References

1. J.-A. Conchello and J. W. Lichtman, "Optical sectioning microscopy," Nat. Methods **2,** 920–931 (2005).
2. J. Lippincott-Schwartz and G. H. Patterson, "Development and use of fluorescent protein markers in living cells," Science **300,** 87–91 (2003).
3. J. W. Lichtman and J.-A. Conchello, "Fluorescence microscopy," Nat. Methods **2,** 910–919 (2005).
4. W. R. Zipfel, R. M. Williams, and W. W. Webb, "Nonlinear magic: multiphoton microscopy in the biosciences," Nature Biotechnol. **21,** 1369–1377 (2003).
5. N. C. Shaner, P. A. Steinbach, and R. Y. Tsien, "A guide to choosing fluorescent proteins," Nat. Methods **2,** 905–909 (2005).
6. P. J. Dwyer, C. A. Dimarzio, J. M. Zavislan, W. J. Fox, and M. Rajadhyaksha, "Confocal reflectance theta line scanning microscope for imaging human skin *in vivo*," Opt. Lett. **31,** 942–944 (2006).
7. J. G. Fujimoto, "Optical coherence tomography for ultrahigh resolution *in vivo* imaging," Nature Biotechnol. **21,** 1361–1367 (2003).

8. L. T. Perelman, V. Backman, M. Wallace, G. Zonios, R. Manoharan, A. Nusrat, S. Shields, M. Seiler, C. Lima, T. Hamano, I. Itzkan, J. Van Dam, J. M. Crawford, and M. S. Feld, "Observation of period find structure in reflectance from biological tissue: a new technique for measuring nuclear size distribution," Phys. Rev. Lett. **80,** 627–630 (1998).
9. I. J. Bigio and J. R. Mourant, "Ultraviolet and visible spectroscopies for tissue diagnostics: fluorescence spectroscopy and elastic-scattering spectroscopy," Phys. Med. Biol. **42,** 803–814 (1997).
10. F. Helmchen and W. Denk, "Deep tissue two-photon microscopy," Nat. Methods **2,** 932–940 (2005).
11. W. R. Zipfel, R. M. Williams, R. Christie, A. Y. Nikitin, B. T. Hyman, and W. W. Webb, "Live tissue intrinsic emission microscopy using multiphoton-excited native fluorescence and second harmonic generation," Proc. Natl. Acad. Sci. U.S.A. **100,** 7075–7080 (2003).
12. E. L. Evan, E. O. Potma, M. Puoris'haag, D. Cote, C. P. Lin, and X. S. Xie, "Chemical imaging of tissue *in vivo* with video-rate coherent anti-Stokes Raman scattering microscopy," Proc. Natl. Acad. Sci. U.S.A. **102,** 16807–16812 (2005).
13. L. H. Laiho, S. Pelet, T. M. Hancewicz, P. D. Kaplan, and P. T. C. So, "Two-photon 3D mapping of *ex vivo* human skin endogenous fluorescence species based on fluorescence emission spectra," J. Biomed. Opt. **10,** 024016 (2005).
14. A. Zoumi, A. Yeh, and B. J. Tromberg, "Imaging cells and extracellular matrix *in vivo* by using second-harmonic generation and two-photon excited fluorescence," Proc. Natl. Acad. Sci. U.S.A. **99,** 11014–1019 (2002).
15. J. X. Cheng, A. Volkmer, and X. S. Xie, "Theoretical and experimental characterization of coherent anti-Stokes Raman scattering microscopy," J. Opt. Soc. Am. B **19,** 1363–1375 (2002).
16. C. Joo, T. Akkin, B. Cense, B. H. Park, and J. F. de Boer, "Spectral-domain optical coherence phase microscopy for quantitative phase-contrast imaging," Opt. Lett. **30,** 2131–2133 (2005).
17. C. Xu, C. Vinegoni, T. S. Ralston, W. Luo, W. Tan, and S. A. Boppart, "Spectroscopic spectra-domain optical coherence microscopy," Opt. Lett. **31,** 1079–1081 (2006).
18. Y. Liu, X. Li, Y. L. Kim, and V. Backman, "Elastic backscattering spectroscopic microscopy," Opt. Lett. **30,** 2445–2447 (2005).
19. V. Backman, M. B. Wallace, L. T. Perelman, J. T. Arendt, R. Gurjar, M. G. Muller, Q. Zhang, G. Zonios, E. Kline, T. McGillican, S. Shapshay, T. Valdez, K. Badizadegan, J. M. Crawford, M. Fitzmaurice, S. Kabani, H. S. Levin, M. Seiler, R. R. Dasari, I. Itzkan, J. Van Dam, and M. S. Feld, "Detection of preinvasive cancer cells," Nature **406,** 35–36 (2000).
20. V. Backman, R. Gurjar, K. Badizadegan, I. Itzkan, R. R. Dasari, L. T. Perelman, and M. S. Feld, "Polarized light scattering spectroscopy for quantitative measurement of epithelial cellular structure *in situ*," IEEE J. Sel. Top. Quantum Electron. **5,** 1019–1026 (1999).
21. M. B. Wallace, L. T. Perelman, V. Backman, J. M. Crawford, M. Fitzmaurice, M. Seiler, K. Badizadegan, S. J. Shields, I. Itzkan, R. R. Dasari, J. V. Dam, and M. S. Feld, "Endoscopic detection of dysplasia in patients with Barrett's esophagus using light scattering spectroscopy," Gastroenterology **119,** 677–682 (2000).
22. V. Backman, V. Gopal, M. Kalashnikov, K. Badizadegan, R. Gurjar, A. Wax, I. Geogakoudi, M. Mueller, C. W. Boone, R. R. Dasari, and M. S. Feld, "Measuring cellular structure at submicrometer scale with light scattering spectroscopy," IEEE J. Sel. Top. Quantum Electron. **7,** 887–893 (2001).
23. R. S. Gurjar, V. Backman, L. T. Perelman, I. Georgakoudi, K. Badizadegan, I. Itzkan, R. R. Dasari, and M. S. Feld, "Imaging human epithelial properties with polarized light-scattering spectroscopy," Nature Med. **7,** 1245–1248 (2001).
24. H. Fang, M. Ollero, E. Vitkin, L. M. Kimerer, P. B. Cipolloni, M. M. Zaman, S. D. Freedman, I. J. Bigio, I. Itzkan, E. B. Hanlon, and L. T. Perelman, "Noninvasive sizing of subcellular organelles with light-scattering spectroscopy," IEEE J. Sel. Top. Quantum Electron. **9,** 267–276 (2003).
25. G. Schuele, E. Vitkin, P. Huie, D. Palanker, and L. T. Perelman, "Optical detection of the reaction of organelles to cellular stress," J. Biomed. Opt. **10,** 051404-1-8 (2005).
26. T. Zimmermann, J. Rietdorf, and R. Pepperkok, "Spectral imaging and its applications in live cell microscopy," FEBS Lett. **546,** 87–92 (2003).
27. W. Weise, P. Zinin, T. Wilson, A. Briggs, and S. Boseck, "Imaging of spheres with the confocal scanning optical microscope," Opt. Lett. **21,** 1800–1802 (1996).
28. J. F. Aguilar, M. Lera, and C. J. R. Sheppard, "Imaging of spheres and surface profiling by confocal microscopy," Appl. Opt. **39,** 4621–4628 (2000).
29. I. J. D. Craig and J. C. Brown, *Inverse Problems in Astronomy: a Guide to Inversion Strategies for Remotely Sensed Data* (Hilger, 1986).
30. R. J. Hanson, "Least squares with bounds and linear constraints," SIAM (Soc. Ind. Appl. Math.) J. Sci. Stat. Comput. **7,** 826–834 (1986).
31. R. J. Hanson, *A Cyclic Reduction Solver for the IMSL Mathematics Library* Report 9002 (International Mathematical and Statistical Library, 1990).
32. T. Wilson and A. R. Carlini, "Size of the detector in confocal imaging systems," Opt. Lett. **12,** 227–229 (1987).
33. E. Marx and G. W. Mulholland, "Size and refractive index determination of single polystyrene spheres," J. Res. Natl. Bur. Stand. **88,** 321–338 (1983).
34. J. S. Bonifacino, M. Dasso, J. B. Hartford, J. Lippincott-Schwartz, and K. M. Yamada, *Current Protocols in Cell Biology* (Wiley, 2001).
35. G. Monika, G. Pal, and J. S. Adam, "Epithelia and bacterial metalloproteinases and their inhibitor in H. pylori infection of human gastric cells," Am. J. Physiol. Gastrointest. Liver Physiol. **281,** 823–832 (2001).
36. M. I. Mishchenko, J. W. Hovenier, and L. D. Travis, *Light Scattering by Nonspherical Particles* (Academic, 2000).